Two-dimensional potential flow solutions with separation

A. VERHOFF†

108 Rosebrook Drive, Florissant, MO 63031, USA

A procedure for constructing two-dimensional incompressible potential flowfield solutions with separation and a recirculation region is presented. It naturally makes use of complex variable theory and other analysis techniques such as conformal mapping and the generalized Poisson integral formula. Flowfield determination is reduced to solution of a boundary value problem in various simple domains. The entire velocity field is described analytically; stream function and velocity potential contour maps are readily constructed. Example solutions are presented. Solutions for sharp leading edge airfoils at arbitrary angle of attack are completely determined, including the limiting angle of attack for upper-surface flow re-attachment. For other configurations (e.g. circular cylinder, backward-facing step) the analytical solution contains one or more free parameters, whose values may be inferred from boundary layer theory or experiment.

---

1. Introduction

For nearly a century the belief has been held (and taught) that viscosity must be taken into account to successfully model, even approximately, flowfields with separation (Lamb 1932; Birkhoff & Zarantonello 1957). Concerning the 'classical hydrodynamics' of an 'ideal fluid', Prandtl & Tietjens (1934) remark: 'This domain has been investigated so thoroughly – particularly by the mathematicians – that we may consider it closed.'

As an example, the classical potential solution (supposedly unique) for uniform flow past a flat-plate airfoil at angle of attack has a circulation component (i.e. lift) that forces the flow to depart smoothly from the trailing edge. Stagnation occurs on the lower surface near the leading edge, with infinite velocity at the leading edge where the velocity vector reverses direction. It has been assumed that no inviscid mechanism is available to remove this singularity. In the real world, so the argument goes, viscosity would produce a blunting effect that would keep leading edge velocity finite and cause leading edge separation for angles of attack greater than some minimal level. The exception to requiring viscous influence is the trivial Helmholtz-type flow (see Birkhoff & Zarantonello 1957; Birkhoff 1960) where adjacent streams having different velocities coexist without mixing (i.e. the mixing layer, or slip line, separating the two streams is infinitely thin and the velocity profile is a step function). One such example is the flow over a backward-facing step, where a region of quiescent fluid lies beneath a region of constant-velocity fluid downstream of the step, extending to infinity; there is no closed recirculation region.

† Email address for correspondence: augustverhoff@sbcglobal.net

Procedures are demonstrated herein for inviscid modelling of a separated, recirculating flow region within an inviscid flowfield taking into account all relevant boundary conditions. The formulation uses velocity magnitude and flow angle as dependent variables. Boundary conditions are imposed primarily in terms of flow angle. The choice of flow angle as a dependent variable leads to a stronger set of boundary conditions for a given problem. At a solid surface the usual inviscid condition of tangential flow (i.e. zero normal velocity) does not fix the velocity direction, leading to the necessity of imposing a Kutta condition (i.e. a circulation) to remove the ambiguity and move a stagnation point to the physically correct location (trailing edge in the case of an airfoil). Additional discussion may be found in Kuethe & Schetzer (1959). Tangential flow with prescribed direction can be imposed when flow angle is used, bypassing the intermediate Kutta condition step, yet producing the same result. Moreover, surface flow angle is geometric and can be determined *a priori* for a particular geometry. Having determined an analytical solution in terms of these variables, the use of complex variable theory allows a straightforward analytical determination of stream function and velocity potential. Stream function contours provide a very useful means of viewing the important features of a given flowfield.

Rigorous analysis of problems using the generalized Poisson integral formula sometimes produces a doublet-like solution element that models separation and the recirculation region. Solution for other closely related configurations can be simplified, in some cases, by superposition of the doublet element boundary conditions and solution onto those of the base problem. Modelling of the recirculation region can also be achieved by a vortex-pair element adding more versatility to the procedure. Within the recirculation region, velocity becomes infinite at the vortical centre, which is characteristic of an inviscid vortex. This is certainly more acceptable than having infinite velocity at an expansion corner (e.g. flat-plate leading edge).

For airfoil shapes producing unsymmetrical flowfields, the periodicity of the solution on any contour enclosing the airfoil must be taken into account. Boundary conditions for the separated flow region in that case are typically expressed in terms of periodic step functions.

Results are presented for uniform flow over a backward-facing step, flow past a circular cylinder with separation, flow over a rectangular cavity and flow past several of a family of sharp leading and trailing edge biconvex airfoils at angle of attack. A flat-plate airfoil is a member of this family (Karman–Trefftz) and results are included for this case. For the backward-facing step, the cavity and the biconvex airfoils at angle of attack, the separation point is fixed, while for the cylinder its location is a free parameter. Circular cylinder flowfield graphics taken from Schlichting (1955) provide for a qualitative comparison of prediction and experiment to provide some assessment of the effects of viscosity. Other demonstrations of the utility of the velocity-flow angle formulation may be found (e.g. Verhoff 1998, 2005).

Much of the research effort in fluid mechanics over the past three decades has been devoted to developing numerical solution methods for various fluid dynamic models (potential flow, Euler equations, Navier–Stokes equations, etc.). There are numerous instances where application of the resulting computational tools has produced remarkable results (see e.g. Jameson 2003). It is hoped that the results presented here that show extension of classical potential flow methods to new problem types might prompt renewed interest in developing simple and efficient engineering tools based on potential theory. Other efforts already underway can be found in Ikeda, Oda, & Shibata (2004) and Yeung & Parkinson (1993).
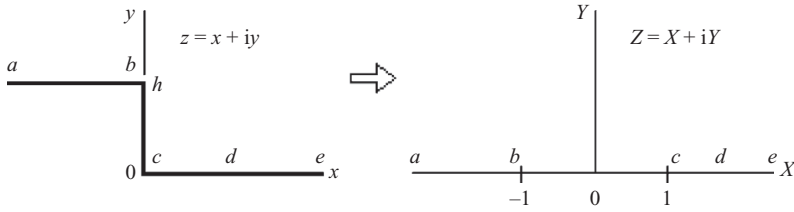
FIGURE 1. Mapping to computational plane.

2. Brief review of potential flow theory and terminology

Two-dimensional incompressible inviscid flow is described in terms of a complex potential Ω, defined in terms of velocity potential Φ and stream function Ψ as

$$\Omega(z) \equiv \Phi + \mathrm{i}\Psi, \quad z \equiv x + \mathrm{i}y. \tag{2.1}$$

Velocity in the physical z plane is obtained from the relation

$$\frac{\mathrm{d}\Omega}{\mathrm{d}z} = q\mathrm{e}^{-\mathrm{i}\theta}, \tag{2.2}$$

where q is velocity magnitude (normalized by free-stream value, q_∞) and θ is flow angle measured with respect to some chosen reference axis (e.g. x-axis). See Kuethe & Schetzer (1959) for additional details.

Velocity potential and stream function have the properties

$$\left. \begin{aligned} \frac{\partial \Phi}{\partial x} &= q \cos\theta = u, & \frac{\partial \Phi}{\partial y} &= q \sin\theta = v, \\ \frac{\partial \Psi}{\partial x} &= -q \sin\theta = -v, & \frac{\partial \Psi}{\partial y} &= q \cos\theta = u, \end{aligned} \right\} \tag{2.3}$$

where u and v are the velocity components in the x and y directions, respectively. Obviously, Φ and Ψ satisfy the Cauchy–Riemann conditions

$$\frac{\partial \Phi}{\partial x} = \frac{\partial \Psi}{\partial y}, \quad \frac{\partial \Phi}{\partial y} = -\frac{\partial \Psi}{\partial x}, \tag{2.4}$$

and therefore each satisfies the (linear) Laplace equation. Superposition can then be used to produce more complicated flowfield descriptions from simple building-block solutions.

The complex dependent variable F is defined as

$$F \equiv \log \left[\frac{\mathrm{d}\Omega}{\mathrm{d}z} \right] = \ln q - \mathrm{i}\theta, \tag{2.5}$$

which conveniently isolates flow angle θ, thereby simplifying the imposition of boundary conditions.

3. Backward-facing step

The classical solution for attached flow over a backward-facing step is obtained from the conformal mapping relation

$$z = \frac{h}{\pi}\{\sqrt{Z^2 - 1} + \log[Z + \sqrt{Z^2 - 1}]\}, \quad Z \equiv X + \mathrm{i}Y, \tag{3.1}$$

where h is the step height. This mapping, from Churchill (1948), is illustrated in figure 1. The parameter h is simply a scaling factor for z. The flowfield for the step
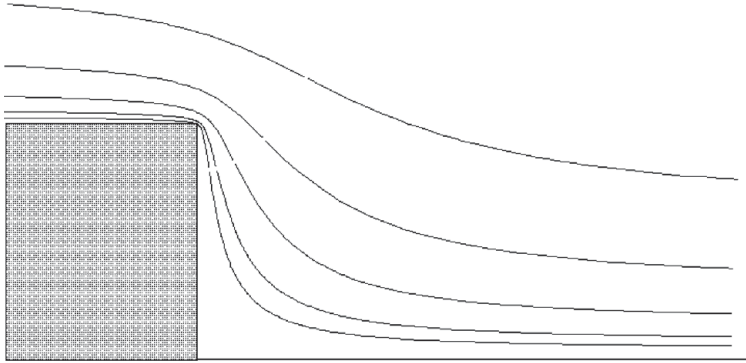
FIGURE 2. Attached flow streamlines.

geometry also represents that of the upper half of the symmetric flow over a semi-infinite constant-thickness body with a square base at $x = 0$. If this thickness is taken as the characteristic dimension, then $h = 1/2$, which will be assumed hereafter. The real and imaginary components of (3.1) are

$$
\left.
\begin{aligned}
x &= \frac{1}{2\pi} \left\{ \sqrt{r} \cos\phi + \frac{1}{2} \ln[(X + \sqrt{r}\cos\phi)^2 + (Y + \sqrt{r}\sin\phi)^2] \right\}, \\
y &= \frac{1}{2\pi} \left\{ \sqrt{r} \sin\phi + \tan^{-1}\left[\frac{Y + \sqrt{r}\sin\phi}{X + \sqrt{r}\cos\phi} \right] \right\},
\end{aligned}
\right\}
\tag{3.2}
$$

where

$$
\left.
\begin{aligned}
r &\equiv \sqrt{(X^2 - Y^2 - 1)^2 + 4X^2 Y^2}, \\
\phi &\equiv \frac{1}{2} \tan^{-1}\left[\frac{2XY}{X^2 - Y^2 - 1} \right] + \frac{\pi}{2}(1 - \mathrm{Sign}[X]).
\end{aligned}
\right\}
\tag{3.3}
$$

Simultaneous numerical inversion of (3.2) provides $X(x, y)$ and $Y(x, y)$. The streamline pattern in the physical z plane is shown in figure 2. Streamlines are images of lines of constant Y in the computational Z plane (i.e. $\Omega \sim Z$).

The derivative of the mapping function (3.1) is

$$
\frac{\mathrm{d}z}{\mathrm{d}Z} = \frac{1}{2\pi} \sqrt{\frac{Z+1}{Z-1}}
\tag{3.4}
$$

so that, from (2.2),

$$
\frac{\mathrm{d}\Omega}{\mathrm{d}z} = 2\pi \frac{\mathrm{d}\Omega}{\mathrm{d}Z} \sqrt{\frac{Z-1}{Z+1}} = q\mathrm{e}^{-\mathrm{i}\theta},
\tag{3.5}
$$

where q and θ are normalized velocity magnitude and flow angle in the z plane. In the far field (i.e. $Z \to \infty$), $q = 1$ and $\theta = 0$ so that

$$
\left. \frac{\mathrm{d}\Omega}{\mathrm{d}Z} \right|_{Z \to \infty} = \frac{1}{2\pi} \quad \text{and} \quad \frac{\mathrm{d}\Omega}{\mathrm{d}z} = \sqrt{\frac{Z-1}{Z+1}}.
\tag{3.6}
$$

Then, from (2.5),

$$
F = \log\left[\frac{\mathrm{d}\Omega}{\mathrm{d}z} \right] = \frac{1}{2} \log\left[\frac{Z-1}{Z+1} \right] = \ln q - \mathrm{i}\theta
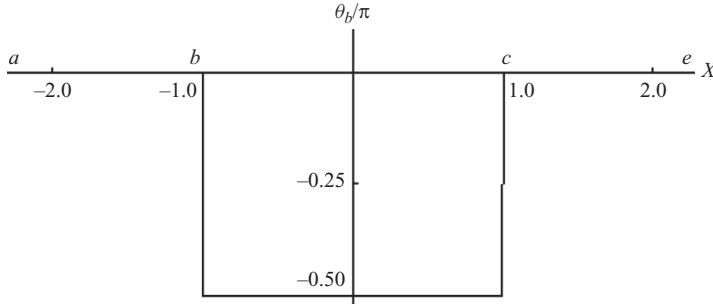\tag{3.7}
$$

FIGURE 3. Surface flow angle (attached flow).

from which q and θ are determined as

$$q = \left[\frac{(X-1)^2 + Y^2}{(X+1)^2 + Y^2}\right]^{1/4}, \quad \theta = \frac{1}{2}\tan^{-1}\left[\frac{Y}{X+1}\right] - \frac{1}{2}\tan^{-1}\left[\frac{Y}{X-1}\right]. \quad (3.8)$$

Stagnation occurs at $Z=1$ while velocity is infinite at $Z=-1$, a physically unrealistic situation. The distribution of surface (boundary) flow angle θ_b mapped to the real axis in the Z plane is shown in figure 3. Note that a factor $\pm 2k\pi$ (k an integer) can be added to θ without altering results obtained from (3.5).

Postulating a recirculation region produced by separation from the corner ($Z=-1$) with subsequent re-attachment at $Z=a$ (denoted as point d in mapping figure 1), surface boundary conditions mapped to the Z plane take the form

$$\theta_b = \begin{cases} 0; & X < -1,\ X > a, \\ \pi/2; & |X| \leqslant 1, \\ -\pi; & 1 \leqslant X \leqslant a. \end{cases} \quad (3.9)$$

Using the generalized Poisson integral formula, the solution for F can be obtained as

$$F(Z) = \frac{1}{\pi} \int_{-\infty}^{\infty} \frac{\theta_b(\sigma)}{Z - \sigma}\,\mathrm{d}\sigma = \frac{1}{2}\log[Z+1] - \frac{3}{2}\log[Z-1] + \log[Z-a]. \quad (3.10)$$

From (2.5), (3.4) and (3.10),

$$\frac{\mathrm{d}\Omega}{\mathrm{d}Z} = \frac{1}{2\pi}\frac{(Z+1)(Z-a)}{(Z-1)^2} \quad (3.11)$$

which integrates to

$$\Omega(Z) = \frac{1}{2\pi}\left\{Z + 2\frac{a-1}{Z-1} + (3-a)\log[Z-1] + \text{const.}\right\}. \quad (3.12)$$

Velocity potential and stream function are, therefore,

$$\left. \begin{aligned} \Phi &= \frac{1}{2\pi}\left\{X + \frac{2(a-1)(X-1)}{(X-1)^2 + Y^2} + \frac{3-a}{2}\ln[(X-1)^2 + Y^2] + \text{const.}\right\}, \\ \Psi &= \frac{1}{2\pi}\left\{Y - \frac{2(a-1)Y}{(X-1)^2 + Y^2} + (3-a)\tan^{-1}\left[\frac{Y}{X-1}\right]\right\}. \end{aligned} \right\} \quad (3.13)$$

A closed recirculation region exists only for $a=3$, since the arctangent produces a step function on the real axis ($Y \to 0^+$) at $X=1$ (i.e. 0 for $X>1$ and π for $X<1$). Retention of this term would preclude the real axis from being the image of the wetting streamline (see figure 1), and the formation of a closed recirculation region.
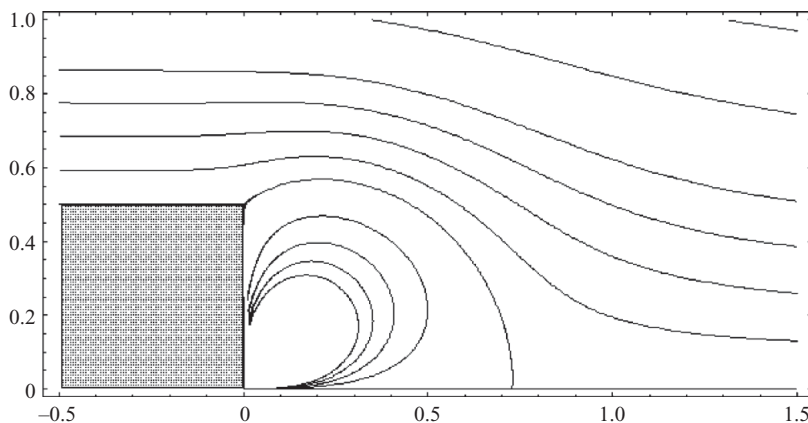
FIGURE 4. Separated flow streamline pattern.

This choice also makes the logarithmic term in (3.12) vanish. With this simplification (3.12) and (3.13) become (after adjustment of the integration constant)

$$\left.\begin{array}{l} \Omega(Z) = \dfrac{1}{2\pi}\left[Z - 1 + \dfrac{4}{Z-1}\right], \\[2ex] \Phi = \dfrac{1}{2\pi}(X - 1)\left[1 + \dfrac{4}{(X-1)^2 + Y^2}\right], \\[2ex] \Psi = \dfrac{1}{2\pi}Y\left[1 - \dfrac{4}{(X-1)^2 + Y^2}\right]. \end{array}\right\} \tag{3.14}$$

These relations are equivalent to those for a doublet (centred at $Z = 1$) superimposed with a uniform flow. A doublet is a combination of a source and sink coalescent at a point. Velocity and flow angle relations obtained from (3.10) are

$$\left.\begin{array}{l} q = \left[\dfrac{(X+1)^2 + Y^2}{(X-1)^2 + Y^2}\right]^{1/4}\sqrt{\dfrac{(X-3)^2 + Y^2}{(X-1)^2 + Y^2}}, \\[3ex] \theta = \dfrac{3}{2}\tan^{-1}\left[\dfrac{Y}{X-1}\right] - \dfrac{1}{2}\tan^{-1}\left[\dfrac{Y}{X+1}\right] - \tan^{-1}\left[\dfrac{Y}{X-3}\right]. \end{array}\right\} \tag{3.15}$$

Stagnation occurs at $Z = -1$ (a characteristic of compressive streamline slope discontinuity) and at $Z = 3$, and velocity becomes infinite at the doublet centre.

Using the inversion relations for (3.2), stream function contours obtained from (3.14) can be mapped to the physical z plane. These are shown in figure 4. Velocity is zero at the external corner and at the re-attachment point. The corresponding $\Phi - \psi$ mesh is presented in figure 5.

Modelling of separation and recirculation by means of a doublet can be generalized for this geometry by rewriting (3.14) as

$$\left.\begin{array}{l} \Omega(Z) = \dfrac{1}{2\pi}\left[Z - p + \dfrac{(1+p)^2}{Z-p}\right], \\[2ex] \Phi = \dfrac{1}{2\pi}(X - p)\left[1 + \dfrac{(1+p)^2}{(X-p)^2 + Y^2}\right], \\[2ex] \Psi = \dfrac{1}{2\pi}Y\left[1 - \dfrac{(1+p)^2}{(X-p)^2 + Y^2}\right], \end{array}\right\} \tag{3.16}$$
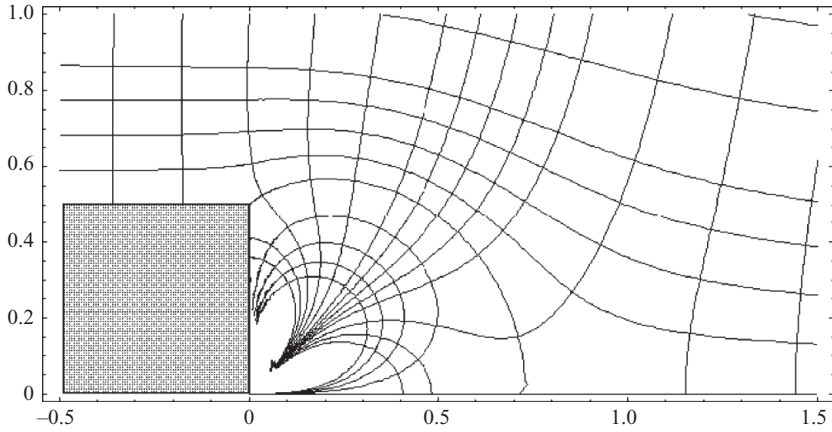
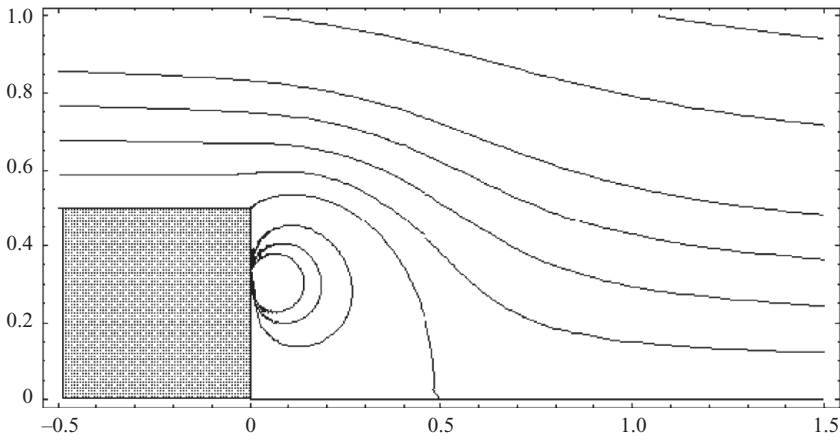FIGURE 5. Velocity potential–stream function mesh.

FIGURE 6. Separated flow streamline pattern ($p = 0.5$).

where $Z = p$ is the arbitrary doublet location. Differentiating Ω,

$$\frac{d\Omega}{dZ} = \frac{1}{2\pi} \frac{(Z+1)(Z-2p-1)}{(Z-p)^2}, \tag{3.17}$$

and using the mapping derivative (3.4),

$$F = \log\left[\frac{d\Omega}{dz}\right] = \log[Z - 2p - 1] + \frac{1}{2}\log[Z+1] + \frac{1}{2}\log[Z-1] - 2\log[Z-p]. \tag{3.18}$$

Physical plane velocity and flow angle are

$$\left.\begin{array}{l} q = \dfrac{\sqrt{(X-2p-1)^2 + Y^2}}{(X-p)^2 + Y^2}\{[(X+1)^2 + Y^2][(X-1)^2 + Y^2]\}^{1/4}, \\[12pt] \theta = 2\tan^{-1}\left[\dfrac{Y}{X-p}\right] - \tan^{-1}\left[\dfrac{Y}{X-2p-1}\right] - \dfrac{1}{2}\tan^{-1}\left[\dfrac{Y}{X+1}\right] - \dfrac{1}{2}\tan^{-1}\left[\dfrac{Y}{X-1}\right]. \end{array}\right\} \tag{3.19}$$

Stream function contours for $p = 0.5$ and $p = 1.5$ are shown in figures 6 and 7, respectively. Velocity is zero at the external corner, at the base and at the re-attachment
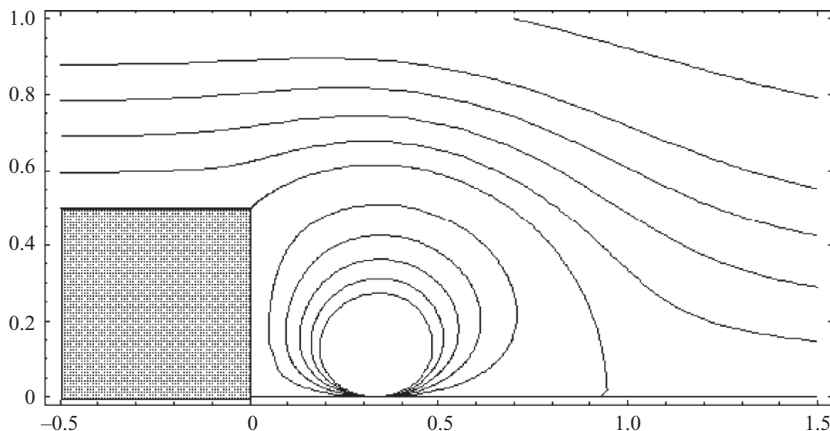
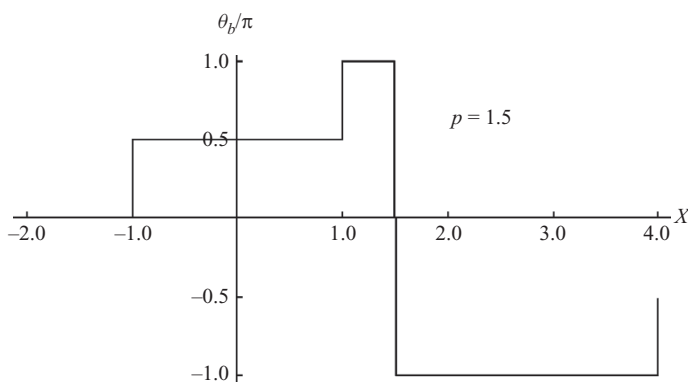FIGURE 7. Separated flow streamline pattern ($p = 1.5$).

FIGURE 8. Surface flow angle (separated flow).

point, $Z = 2p + 1$, and infinite at the doublet location $Z = p$. Boundary flow angle θ_b mapped to the real axis in the Z plane is shown in figure 8 for $p = 1.5$. The fact that θ can be adjusted by $\pm 2k\pi$ is evident in this figure. The re-attachment point in the z plane is obtained from the mapping relation (3.1) as

$$x_a(p) = \frac{1}{2\pi}\{\sqrt{(2p+1)^2 - 1} + \ln[2p + 1 + \sqrt{(2p+1)^2 - 1}]\}. \qquad (3.20)$$

Separation with recirculation can also be modelled by a vortex pair whose complex potential is

$$\Omega(Z) = \frac{1}{2\pi}\left\{Z - p - i\frac{(p+1)^2 + s^2}{2s}\log\left[\frac{Z - p + is}{Z - p - is}\right]\right\}, \qquad (3.21)$$

where the vortices are located at $Z = p \pm is$. See Rauscher (1953) for additional details. Velocity potential and stream function are

$$\left.\begin{array}{l}\Phi = \dfrac{1}{2\pi}\left\{X - p + \dfrac{(p+1)^2 + s^2}{2s}\left[\tan^{-1}\left(\dfrac{Y+s}{X-p}\right) - \tan^{-1}\left(\dfrac{Y-s}{X-p}\right)\right]\right\}, \\[4mm] \Psi = \dfrac{1}{2\pi}\left\{Y - \dfrac{(p+1)^2 + s^2}{4s}\ln\left[\dfrac{(X-p)^2 + (Y+s)^2}{(X-p)^2 + (Y-s)^2}\right]\right\}.\end{array}\right\} \qquad (3.22)$$
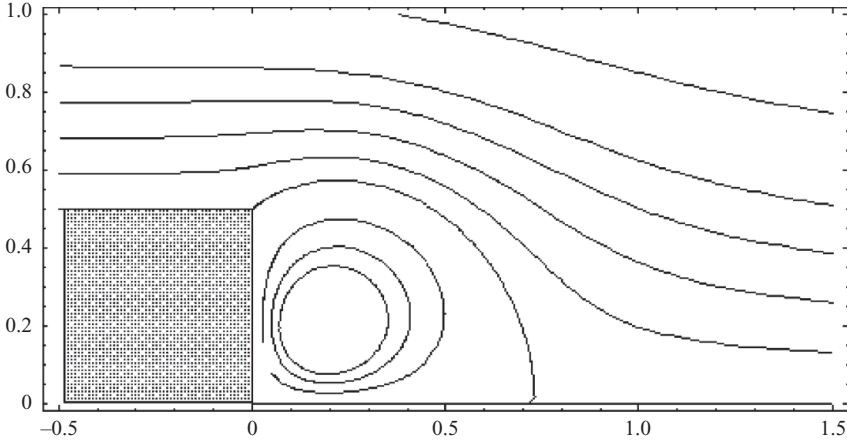
FIGURE 9. Separated flow streamline pattern ($p = 1.0$, $s = 0.35$).

The left-hand stagnation point (i.e. the image of the external corner) is at $Z = -1$, while the right-hand stagnation point (i.e. the re-attachment point) is at $Z = 2p + 1$, as was the case for the doublet model.

The derivative of (3.21) when combined with the mapping derivative (3.4) gives

$$\frac{d\Omega}{dz} = \frac{(Z - 2p - 1)\sqrt{Z + 1}\sqrt{Z - 1}}{(Z - p + is)(Z - p - is)}, \tag{3.23}$$

which provides the velocity and flow angle relations

$$\left.\begin{aligned}
q &= \sqrt{\frac{(X - 2p - 1)^2 + Y^2}{[(X - p)^2 + (Y + s)^2][(X - p)^2 + (Y - s)^2]}} \\
&\quad \times \{[(X + 1)^2 + Y^2][(X - 1)^2 + Y^2]\}^{1/4}, \\
\theta &= \tan^{-1}\left[\frac{Y + s}{X - p}\right] + \tan^{-1}\left[\frac{Y - s}{X - p}\right] - \tan^{-1}\left[\frac{Y}{X - 2p - 1}\right] \\
&\quad - \frac{1}{2}\tan^{-1}\left[\frac{Y}{X + 1}\right] - \frac{1}{2}\tan^{-1}\left[\frac{Y}{X - 1}\right].
\end{aligned}\right\} \tag{3.24}$$

Stream function contours for $p = 1.0$ and $s = 0.35$ are shown in figure 9. Velocity is finite everywhere except at the vortex centres, $Z = p \pm is$. The distribution of surface flow angle θ_b mapped to the real axis in the Z plane is shown in figure 10. Note, as was pointed out previously, the equivalence of flow angles 0 and -2π, along with $\pi/2$ and $-3\pi/2$. Even though there appears to be quadrant ambiguity, $\sin\theta$ and $\cos\theta$ behave properly for calculation of longitudinal and lateral velocity components. The re-attachment point in the z plane for the vortex-pair model is also given by (3.20).

The vortex-pair model (3.21) has two free parameters (i.e. p and s), while the doublet model (3.16) has only one (i.e. p). Streamline patterns for the two models are qualitatively similar outside of the recirculation regions (compare figures 4 and 9). The vortex-pair model gives a clearer definition of the recirculation region, but is slightly more difficult to implement computationally. In the limit of vanishing s, the two models are equivalent.
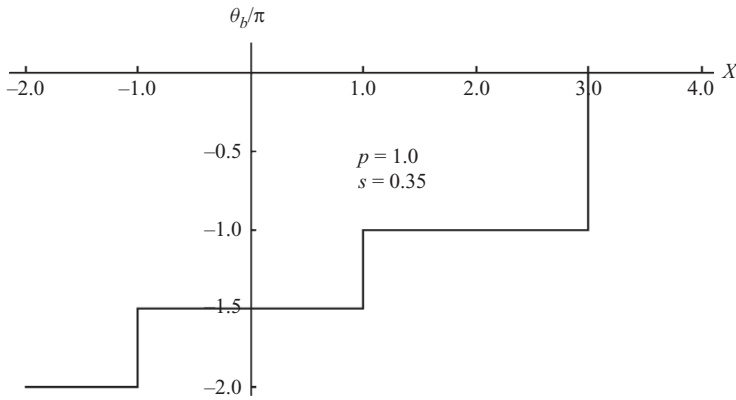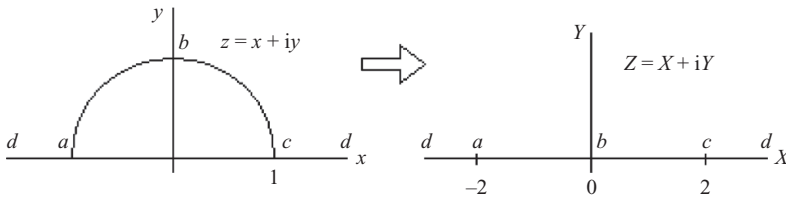
FIGURE 10. Surface flow angle (separated flow).

FIGURE 11. Mapping to computational plane.

4. Circular cylinder

Because of their somewhat similar nature, solution elements and procedures for the backward-facing step problem carry over to construction of the solution for flow past a circular cylinder with separation, bypassing solution via the generalized Poisson integral formula. In general, this is not the case. Vertical symmetry for the cylinder flowfield will be assumed.

The familiar Joukowsky mapping

$$Z = z + \frac{1}{z}, \quad Z = X + iY \tag{4.1}$$

collapses the unit semicircle onto the real axis in the computational Z plane, as shown in figure 11. Real and imaginary component relations are

$$X = x + \frac{x}{x^2 + y^2}, \quad Y = y - \frac{y}{x^2 + y^2}. \tag{4.2}$$

The inverse relations are

$$x = \tfrac{1}{2}[X + \sqrt{\rho}\cos\psi], \quad y = \tfrac{1}{2}[Y + \sqrt{\rho}\sin\psi], \tag{4.3}$$

where

$$\left.\begin{array}{l} \rho \equiv \sqrt{(X^2 - Y^2 - 4)^2 + 4X^2Y^2}, \\[2mm] \psi \equiv \dfrac{1}{2}\tan^{-1}\left[\dfrac{2XY}{X^2 - Y^2 - 4}\right] + \dfrac{\pi}{2}(1 - \text{Sign}[X]). \end{array}\right\} \tag{4.4}$$
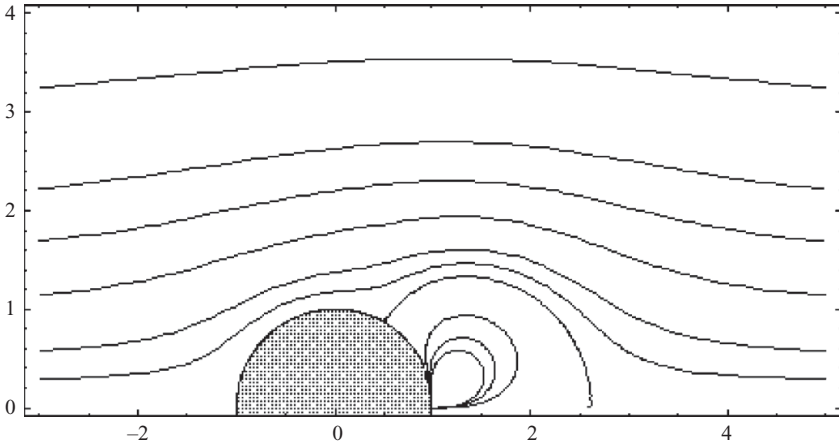
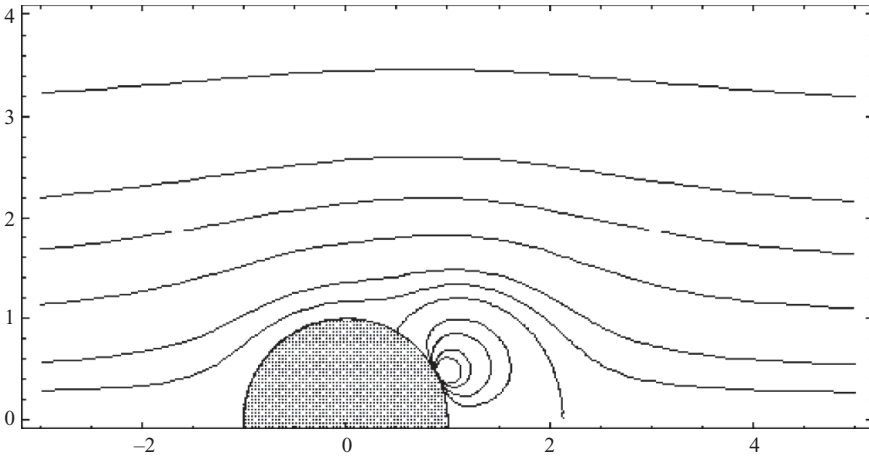FIGURE 12. Separated flow streamline pattern ($p = 2, b = 1$).

FIGURE 13. Separated flow streamline pattern ($p = 1.8, b = 1$).

Modelling of separation and recirculation can be achieved using a further generalization of the doublet model (3.16), namely

$$\left.\begin{aligned}
\Omega(Z) &= Z - p + \frac{(p-b)^2}{Z-p}, \\
\Phi &= (X - p)\left[1 + \frac{(p-b)^2}{(X-p)^2 + Y^2}\right], \\
\Psi &= Y\left[1 - \frac{(p-b)^2}{(X-p)^2 + Y^2}\right],
\end{aligned}\right\} \tag{4.5}$$

where $Z = p$ is again the doublet location and $Z = b$ is the separation point. Since the separation point is not fixed, as was the case for the backward-facing step, the doublet model has two free parameters for this application. Stream function can be mapped back to the physical plane using the component relations (4.2).

Stream function contours for the parameter combinations ($p = 2, b = 1$), ($p = 1.8, b = 1$) and ($p = 2.2, b = 1.5$) are shown in figures 12–14. The separation
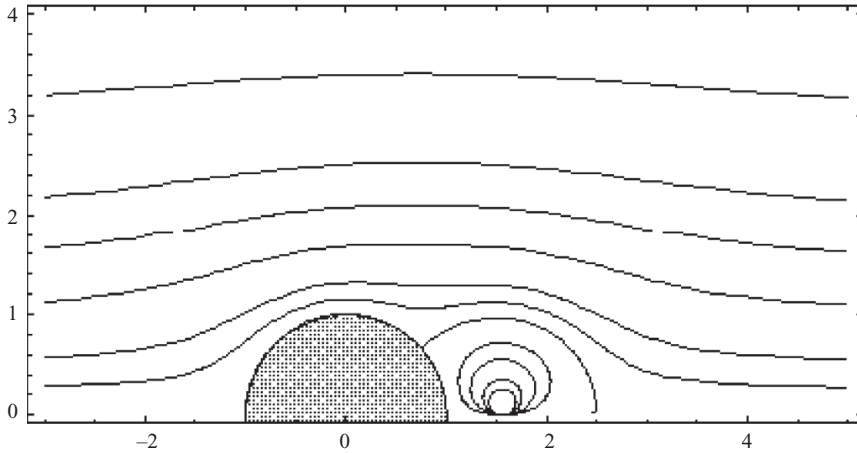
FIGURE 14. Separated flow streamline pattern ($p = 2.2$, $b = 1.5$).

and re-attachment points as obtained from (4.2) are

$$\left.\begin{aligned} x_b &= \frac{b}{2}, \\ x_a &= \tfrac{1}{2}[2p - b + \sqrt{(2p - b)^2 - 4}]. \end{aligned}\right\} \tag{4.6}$$

From (4.1) and (4.5), the derivatives of the mapping function and Ω are

$$\frac{dZ}{dz} = \frac{1}{2}[Z\sqrt{Z^2 - 4} - Z^2 + 4], \quad \frac{d\Omega}{dZ} = \frac{(Z - b)(Z - 2p + b)}{(Z - p)^2}, \tag{4.7}$$

which combine to give

$$\frac{d\Omega}{dz} = \frac{1}{2}[Z\sqrt{Z^2 - 4} - Z^2 + 4]\frac{(Z - b)(Z - 2p + b)}{(Z - p)^2}. \tag{4.8}$$

The first factor in this result pertains to the attached-flow solution for the cylinder, and can be expressed in terms of real and imaginary parts as

$$\tfrac{1}{2}[Z\sqrt{Z^2 - 4} - Z^2 + 4] = \tfrac{1}{2}[\sqrt{\rho}(X\cos\psi - Y\sin\psi) - X^2 + Y^2 + 4]$$
$$+ \tfrac{i}{2}[\sqrt{\rho}(Y\cos\psi + X\sin\psi) - 2XY]. \tag{4.9}$$

This provides the attached-flow field solutions for q and θ, namely

$$\left.\begin{aligned} q_o &= \tfrac{1}{2}\sqrt{[\sqrt{\rho}(X\cos\psi - Y\sin\psi) - X^2 + Y^2 + 4]^2 + [\sqrt{\rho}(Y\cos\psi + X\sin\psi) - 2XY]^2}, \\ \theta_o &= -\tan^{-1}\left[\frac{\sqrt{\rho}(Y\cos\psi + X\sin\psi) - 2XY}{\sqrt{\rho}(X\cos\psi - Y\sin\psi) - X^2 + Y^2 + 4}\right]. \end{aligned}\right\} \tag{4.10}$$

On the real axis ($Y = 0$),

$$\theta_o(X, 0) = \begin{cases} -\tan^{-1}\left[\dfrac{X}{\sqrt{4 - X^2}}\right]; & |X| \leqslant 2, \\ 0; & |X| > 2, \end{cases} \tag{4.11}$$
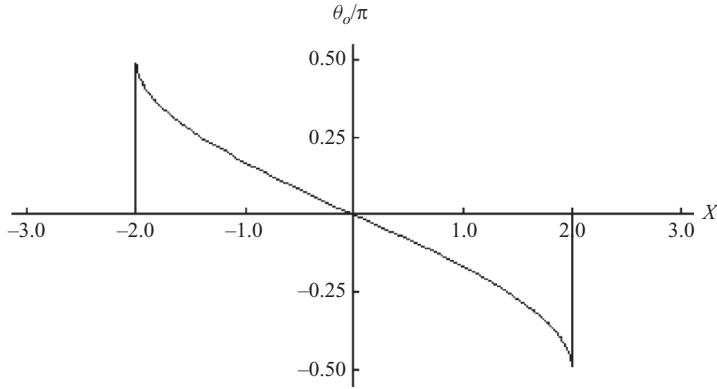
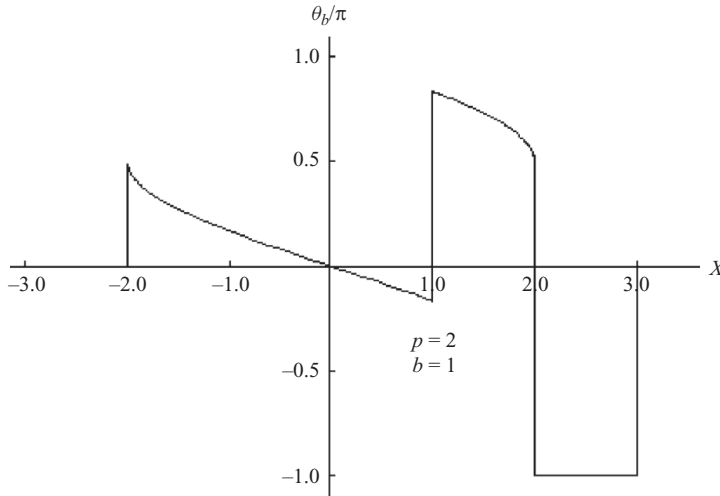FIGURE 15. Surface variation of θ_o (attached flow).

FIGURE 16. Surface flow angle (separated flow).

For the separated flow situation, q and θ are obtained from (4.8) as

$$\left.\begin{aligned} q &= q_o \frac{\sqrt{[(X-b)^2 + Y^2][(X-2p+b)^2 + Y^2]}}{[(X-p)^2 + Y^2]}, \\ \theta &= \theta_o + 2\tan^{-1}\left[\frac{Y}{X-p}\right] - \tan^{-1}\left[\frac{Y}{X-b}\right] - \tan^{-1}\left[\frac{Y}{X-2p+b}\right]. \end{aligned}\right\} \tag{4.12}$$

The distribution of θ_o along the real axis in the Z plane (i.e. $Y=0$) obtained from (4.10) or (4.11) is shown in figure 15. The separated-flow distribution for $p=2$, $b=1$ obtained from (4.12) is shown in figure 16. These two figures illustrate the ease with which boundary conditions in terms of flow angle can be implemented. The distribution of q for the same conditions is shown in figure 17. (The coordinate X has been parametrically replaced by arc length σ). Velocity becomes infinite at the doublet centre location. The attached-flow velocity q_o is also shown for reference; the classical sine function variation on the cylinder surface is evident.
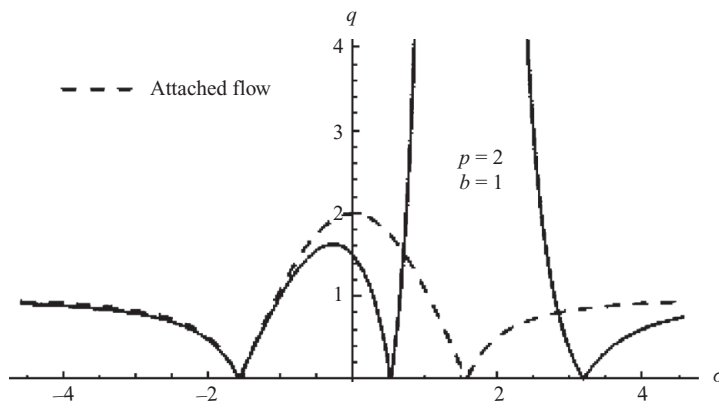
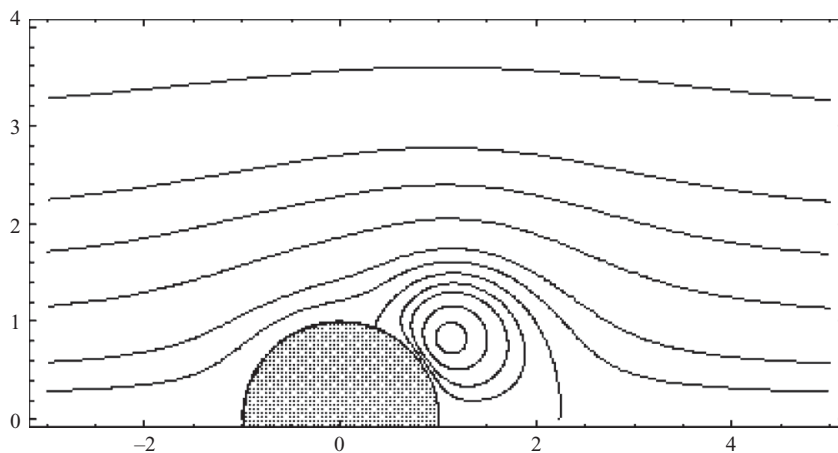FIGURE 17. Boundary distribution of velocity.

FIGURE 18. Separated flow streamline pattern ($p = 1.7, b = 0.7, s = 0.4$).

The separation and recirculation region for the cylinder can also be modelled by slightly modifying the vortex-pair model (3.21) in the form

$$\Omega(Z) = Z - p - i\frac{(p - b)^2 + s^2}{2s} \log \left[\frac{Z - p + is}{Z - p - is} \right]. \tag{4.13}$$

The vortex centres are again at $Z = p \pm is$ and $Z = b$ is the separation point location. The model has three free parameters. The re-attachment point is at $Z = 2p - b$. Velocity potential and stream function are

$$\left. \begin{aligned} \Phi &= X - p + \frac{(p - b)^2 + s^2}{2s} \left\{ \tan^{-1} \left[\frac{Y + s}{X - p} \right] - \tan^{-1} \left[\frac{Y - s}{X - p} \right] \right\}, \\ \Psi &= Y - \frac{(p - b)^2 + s^2}{4s} \ln \left[\frac{(X - p)^2 + (Y + s)^2}{(X - p)^2 + (Y - s)^2} \right]. \end{aligned} \right\} \tag{4.14}$$

Stream function contours for the parameter combinations ($p = 1.7, b = 0.7, s = 0.4$) and ($p = 2.1, b = 0.7, s = 0.3$) are shown in figures 18 and 19. The separation and re-attachment points are also given by (4.6).

Schlichting (1955) provides summary details from a boundary-layer solution which predicts the separation point for a circular cylinder to be at approximately 70° polar
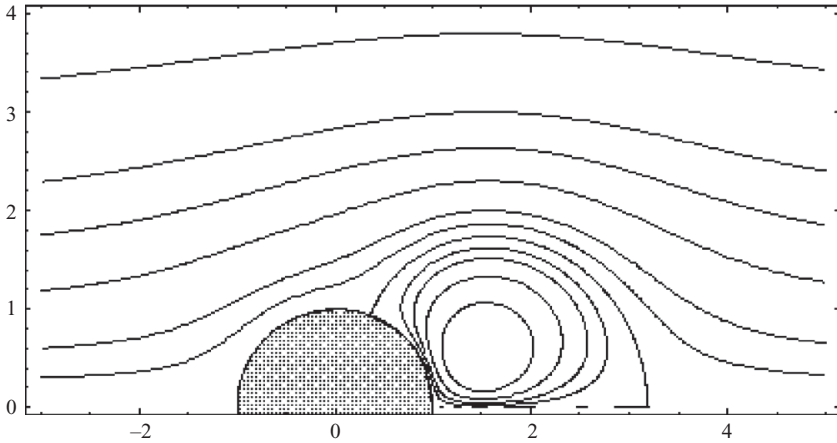
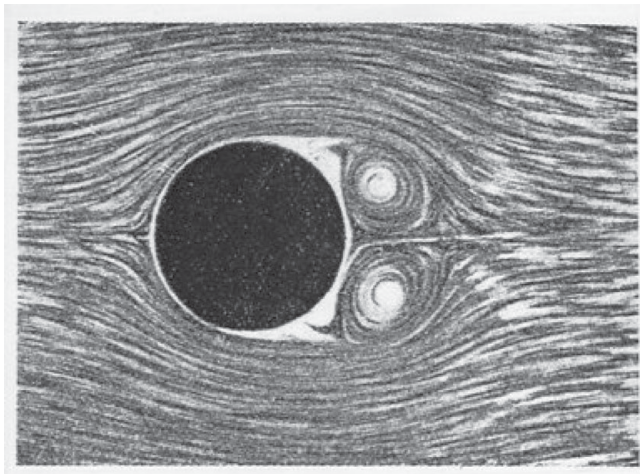FIGURE 19. Separated flow streamline pattern ($p = 2.1$, $b = 0.7$, $s = 0.3$).

FIGURE 20. Flow visualization graphic.

angle. Using (4.6), the corresponding value of b is approximately 0.7. Flow visualization graphics from Schlichting (1955, p. 192, figures 11.5d and 11.5e) are presented in figures 20 and 21. The cylinder velocity (and Reynolds number) for the two graphics are different, but they can be compared with the inviscid predictions of figures 18 and 19. Although any comparison must be strictly qualitative, adjustment of the parameters p and s gives a reasonable likeness of the major flowfield features. Additional flow visualization graphics can be found in Goldstein (1957, plates 7, 8 and 31), which provide further qualitative support for the separation model presented above.

5. Biconvex airfoils

The Karman–Trefftz family of biconvex airfoils is mapped to the unit circle in the w plane by the transformation

$$\frac{z-2}{z+2} = \left(\frac{w-1}{w+1}\right)^{2-\tau/\pi}, \qquad w \equiv u + iv, \tag{5.1}$$
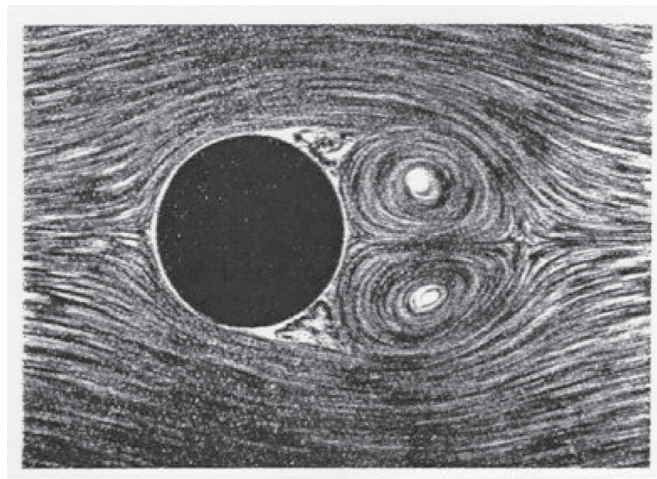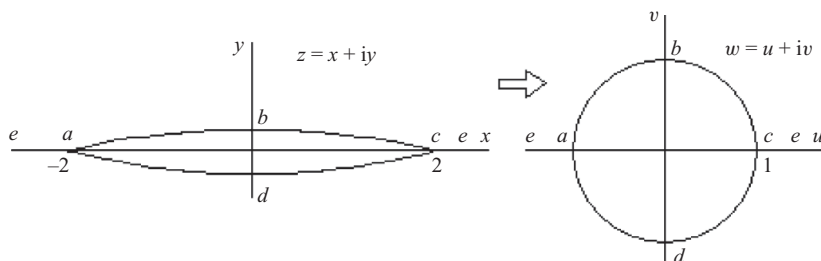
FIGURE 21. Flow visualization graphic.

FIGURE 22. Mapping to unit circle plane.

where τ is the leading/trailing edge angle. The mapping of these sharp leading/trailing edge shapes is illustrated in figure 22. When $\tau = 0$, (5.1) reduces to the classical flat plate to unit circle mapping. The general Karman–Trefftz mapping, as described in Rauscher (1953), allows for a blunt leading edge, camber and finite trailing edge angle.

Inversion of the mapping relation (5.1) gives

$$\frac{w-1}{w+1} = \left(\frac{z-2}{z+2}\right)^{\pi/(2\pi-\tau)} , \quad \lim_{z \to \infty}\left(\frac{w}{z}\right) = \frac{2\pi - \tau}{2\pi} \tag{5.2}$$

from which the mapping derivative is obtained in mixed form as

$$\frac{\mathrm{d}w}{\mathrm{d}z} = \frac{2\pi}{2\pi - \tau} \frac{(w+1)(w-1)}{(z+2)(z-2)}. \tag{5.3}$$

The component surface mapping can be derived from (5.1) in the form

$$x(\beta) = \frac{2(1-\lambda^2)}{1+\lambda^2 - 2\lambda\cos\mu} , \quad y(\beta) = \frac{4\lambda\sin\mu}{1+\lambda^2 - 2\lambda\cos\mu}, \tag{5.4}$$

where

$$\lambda(\beta) \equiv \left[\frac{1-\cos\beta}{1+\cos\beta}\right]^{1-\tau/2\pi} , \quad \mu(\beta) \equiv \left(\pi - \frac{\tau}{2}\right)\mathrm{Sign}[\pi - \beta] \tag{5.5}$$

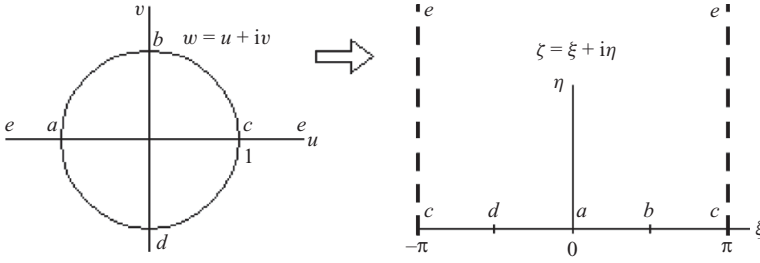254   *A. Verhoff*
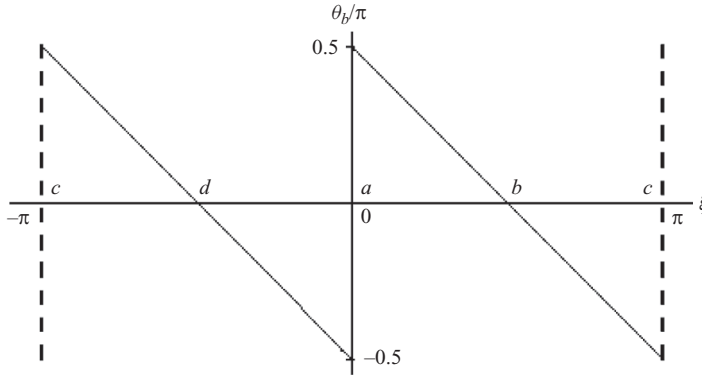

FIGURE 23. Mapping to periodic plane.

FIGURE 24. Boundary flow angle (attached flow).

and β is the unit circle polar angle. From (5.2) the real and imaginary components of w can be obtained as

$$u(x,y) = \frac{1-R^2}{1+R^2-2R\cos\omega}, \quad v(x,y) = \frac{2R\sin\omega}{1+R^2-2R\cos\omega}, \quad (5.6)$$

where

$$R \equiv \left[\frac{\sqrt{(x^2+y^2-4)^2+16y^2}}{(x+2)^2+y^2}\right]^{\pi/(2\pi-\tau)}, \quad \omega \equiv \frac{\pi}{2\pi-\tau}\tan^{-1}\left[\frac{4y}{x^2+y^2-4}\right]. \quad (5.7)$$

To properly model a leading-edge separation bubble for the case where the biconvex airfoil is at angle of attack, the w plane must be mapped to the periodic ζ plane to account for flowfield periodicity. This mapping, from Churchill (1948), is

$$w = -e^{-i\zeta}, \quad \zeta \equiv \xi + i\eta, \quad (5.8)$$

and is illustrated in figure 23.

Because of the simplicity of this mapping, an efficient solution strategy consists of deriving the unit circle solution in the periodic ζ plane and then transform to the w plane by means of (5.8). Surface flow angle boundary conditions for attached uniform flow past the circle are shown in figure 24. The periodic harmonic function whose imaginary part has this saw-tooth boundary distribution is

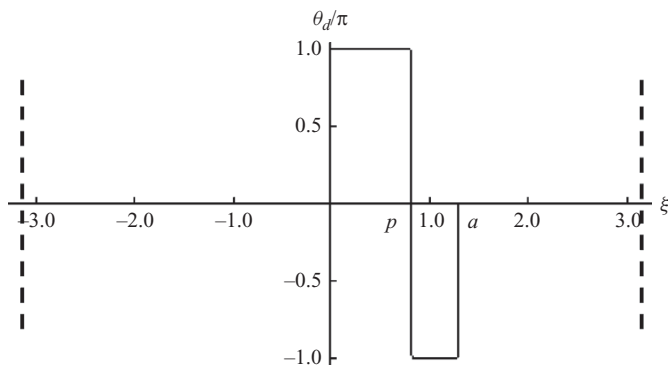$$F_o = \ln q - i\theta = \log[1+e^{i\zeta}] + \log[1-e^{i\zeta}], \quad (5.9)$$

FIGURE 25. Boundary flow angle (doublet).

where q and θ are velocity and flow angle in the unit circle flowfield. In terms of w,

$$\ln q - i\theta = \log\left[\frac{d\Omega}{dw}\right] = \log\left[1 - \frac{1}{w^2}\right],\qquad(5.10)$$

so that the complex potential for attached flow has the familiar form

$$\Omega_o = \Phi_o + i\Psi_o = w + \frac{1}{w}.\qquad(5.11)$$

Referring to the previous analyses, modelling of leading edge separation with recirculation by a doublet-like element requires a boundary flow angle distribution as shown in figure 25. The doublet is centred at $\zeta = p$ with separation at $\zeta = 0$ and re-attachment at $\zeta = a$. This distribution is a combination of three step functions, and the periodic harmonic function whose imaginary part has this boundary distribution is

$$F_d = \log[1 - e^{i(\zeta-a)}] - 2\log[1 - e^{i(\zeta-p)}] + \log[1 - e^{i\zeta}] - i\left(p - \frac{a}{2}\right).\qquad(5.12)$$

Introducing the mapping (5.8) and superimposing with (5.10) gives the unit circle solution with separation

$$\ln q - i\theta = \log\left[\frac{d\Omega}{dw}\right] = \log\left[e^{-i\alpha}\frac{1}{w^2}\frac{(w-1)(w+1)^2(w+e^{-i a})}{(w+e^{-i p})^2}\right].\qquad(5.13)$$

Evaluation of (5.12) in the far field (i.e. for large η), defines the induced angle of attack as

$$\alpha \equiv p - \frac{a}{2}.\qquad(5.14)$$

From (5.13),

$$\frac{d\Omega}{dw} = e^{-i\alpha}\frac{1}{w^2}\frac{(w-1)(w+1)^2(w+e^{-i a})}{(w+e^{-i p})^2},\qquad(5.15)$$

which is readily integrated to give the complex potential in the w plane. One of the resulting terms has the logarithmic form $\log[1 + e^{i p}w]$, whose coefficient must vanish in order that a closed recirculation region be produced. A similar situation arose in
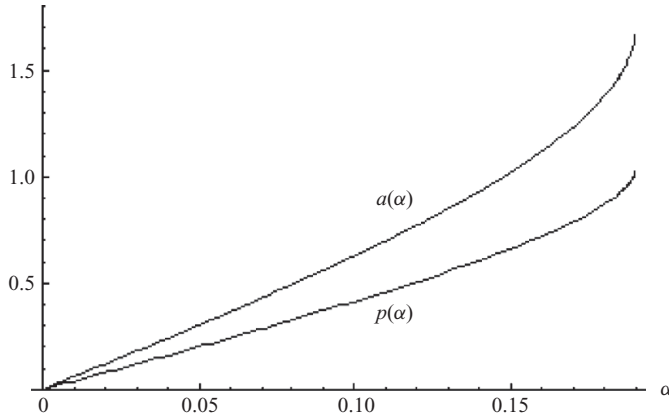
FIGURE 26. Doublet location and re-attachment point.

the backward-facing step analysis, leading to (3.14). This requires the condition

$$\cos\left(\frac{a}{2}\right)\cos p - \cos\left(\frac{a}{2} - 2p\right) = 0. \tag{5.16}$$

The complex potential is then

$$\Omega = w\mathrm{e}^{-\mathrm{i}\alpha} + \frac{\mathrm{e}^{\mathrm{i}\alpha}}{w} - \frac{4\mathrm{i}\sin p[\cos(p-\alpha) - \cos\alpha]}{1 + \mathrm{e}^{\mathrm{i}p}w}$$
$$+ \mathrm{i}[2\sin(p+\alpha) - \sin(2p-\alpha) - \sin\alpha]\log w + \mathrm{const.} \tag{5.17}$$

Relations (5.14) and (5.16) have been used to simplify coefficients. The integration constant can be selected so that $\Psi = 0$ coincides with the surface streamline.

Simultaneous solution of (5.14) and (5.16) allows the parameters p (doublet location) and a (re-attachment point location) to be expressed as functions of the free parameter α (i.e. angle of attack). These relations are shown in figure 26. For values of α greater than approximately 0.19 ($\sim 11°$), solutions do not exist, which implies that for such values of α the flow does not re-attach. The limiting numerical values of p and a are 1.029 and 1.677, respectively. Referring to (5.8) and (5.14) and figures 23 and 25, the re-attachment point can be related to the unit circle polar angle β by

$$\xi = a = 2p - 2\alpha, \quad w = \mathrm{e}^{\mathrm{i}\beta_a} = -\mathrm{e}^{-2\mathrm{i}(p-\alpha)}, \quad \beta_a = \pi - 2p - 2\alpha. \tag{5.18}$$

Physical plane surface coordinates can then be obtained from (5.4).

Velocity potential and stream function can be obtained from (5.17) as

$$\left.\begin{aligned}
\Phi &= (u\cos\alpha + v\sin\alpha)(g+1) - [2\sin(p+\alpha) - \sin(2p-\alpha) - \sin\alpha]\tan^{-1}\left[\frac{v}{u}\right] \\
&\quad - 4\sin p[\cos(p-\alpha) - \cos\alpha](u\sin p + v\cos p)\,f, \\
\Psi &= (u\sin\alpha - v\cos\alpha)(g-1) - \tfrac{1}{2}[2\sin(p+\alpha) - \sin(2p-\alpha) - \sin\alpha]\ln g \\
&\quad - 4\sin p\,[\cos(p-\alpha) - \cos\alpha](1 + u\cos p - v\sin p)f \\
&\quad + 2\sin p[\cos(p-\alpha) - \cos\alpha], \\
f &\equiv [(1 + u\cos p - v\sin p)^2 + (u\sin p + v\cos p)^2]^{-1}; \quad g \equiv (u^2 + v^2)^{-1}.
\end{aligned}\right\} \tag{5.19}$$
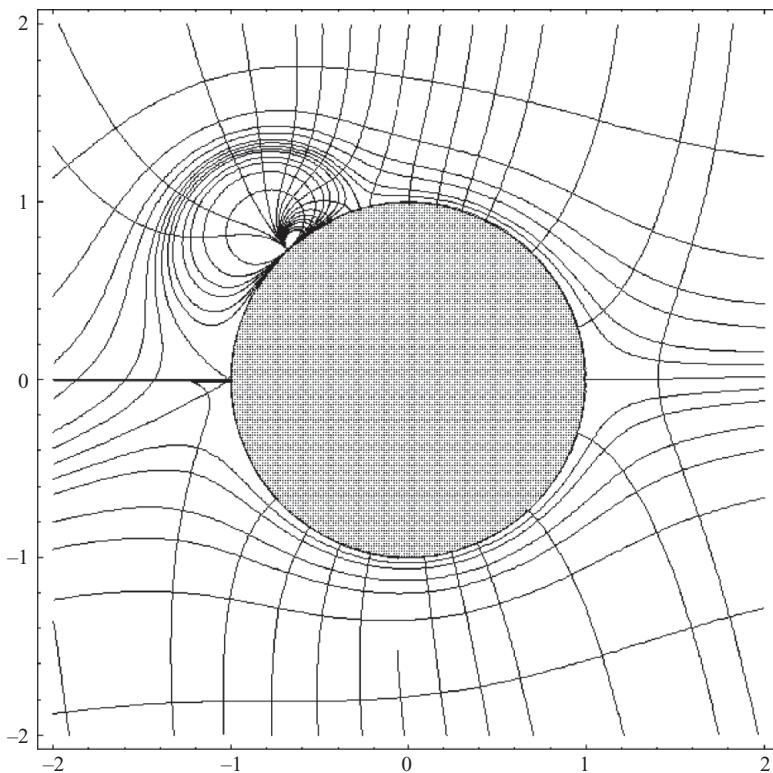
FIGURE 27. Velocity potential–stream function mesh ($\alpha = 10°$).
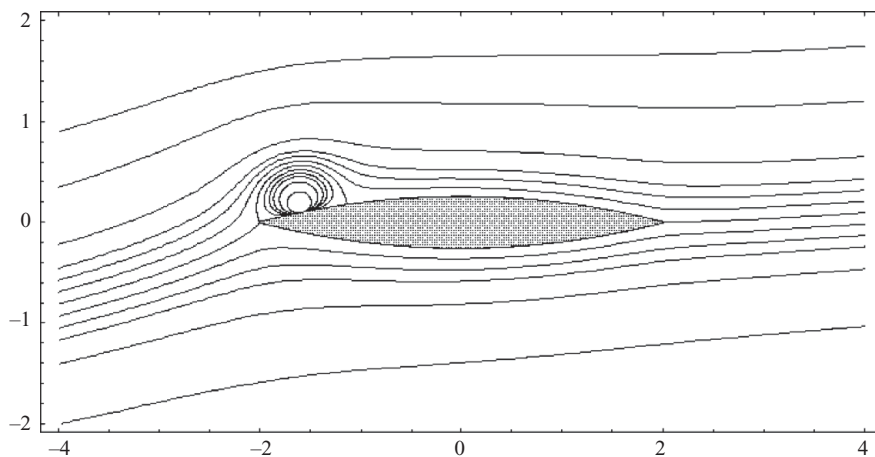
FIGURE 28. Separated flow streamline pattern ($\tau = .50, \alpha = 8°$).

The velocity potential–stream function mesh in the w plane obtained from (5.19) is shown in figure 27 for $\alpha = 10°$. Using (5.6), stream function contours for any of the family of biconvex airfoils can be mapped to the physical plane as shown in figures 28–31. Figures 28 and 29 show contours for $\tau = 0.50$ at $\alpha = 8°$ and $11°$. Figures 30 and 31 show contours at $\alpha = 11°$ for $\tau = 0.25$ and $\tau = 0$ (i.e. flat plate). The velocity
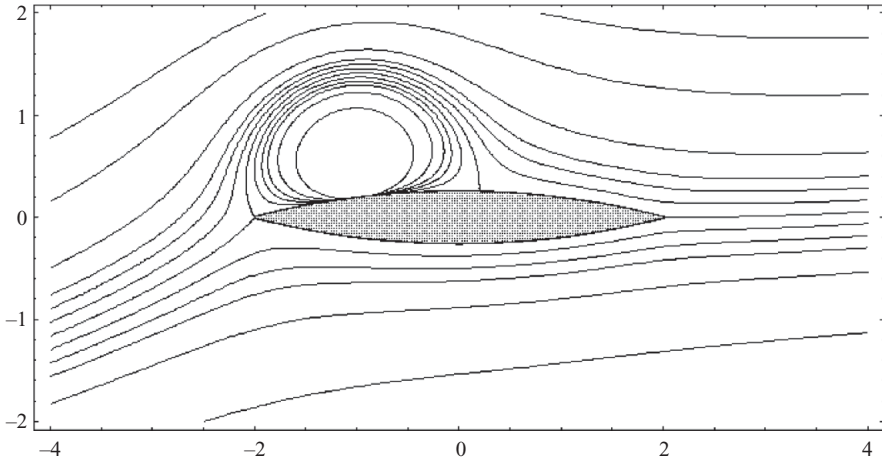
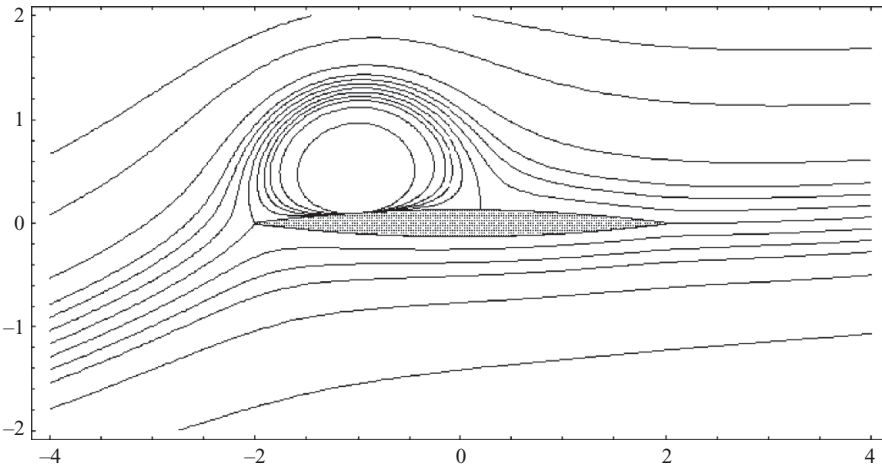FIGURE 29. Separated flow streamline pattern ($\tau = .50$, $\alpha = 11°$).

FIGURE 30. Separated flow streamline pattern ($\tau = .25$, $\alpha = 11°$).

potential–stream function mesh in the z plane is shown in figure 32 for $\tau = 0.50$ and $\alpha = 11°$.

Velocity and flow angle in the physical plane can be obtained by combining the mapping derivative (5.3) and (5.13), with the result

$$\ln q - \mathrm{i}\theta = \log \left[\frac{\mathrm{d}\Omega}{\mathrm{d}w} \right] + \log \left[\frac{\mathrm{d}w}{\mathrm{d}z} \right] = \log \left[\mathrm{e}^{-\mathrm{i}\alpha} \frac{1}{w^2} \frac{(w-1)(w+1)^2(w+\mathrm{e}^{-\mathrm{i}a})}{(w+\mathrm{e}^{-\mathrm{i}p})^2} \right]$$

$$+ \log \left[\left(\frac{2\pi}{2\pi - \tau} \right)^2 \frac{(w+1)(w-1)}{(z+2)(z-2)} \right], \quad (5.20)$$

where w is expressed in terms of x and y by means of (5.6). A constant term has been added to account for the far-field behaviour noted in (5.2). The real and imaginary
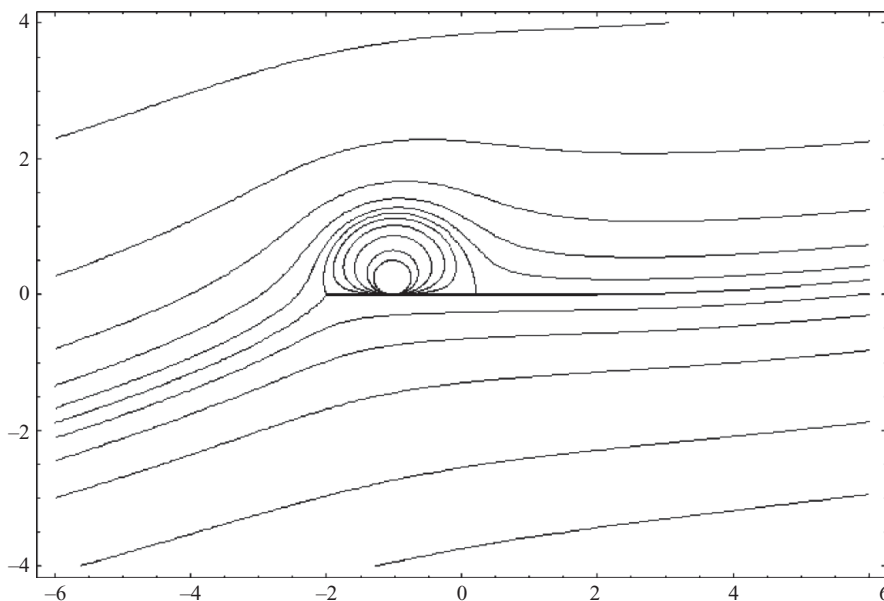
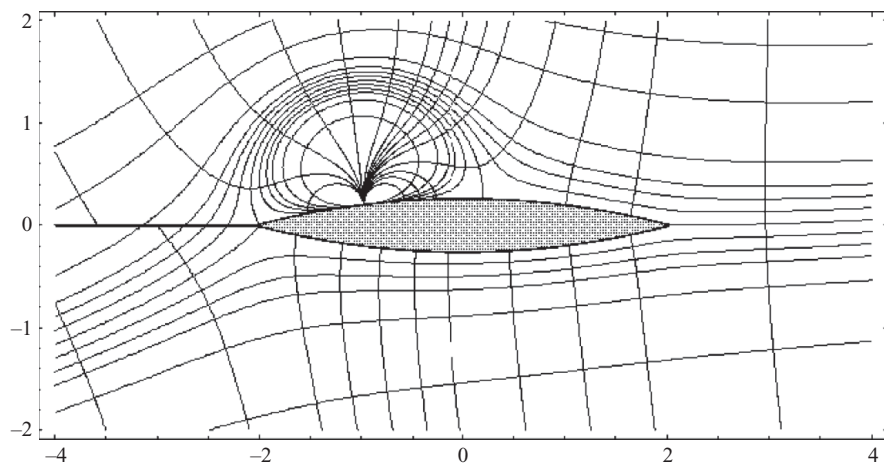FIGURE 31. Separated flow streamline pattern ($\tau = 0$, $\alpha = 11°$).

FIGURE 32. Velocity potential–stream function mesh ($\tau = .50$, $\alpha = 11°$).

parts of (5.20) yield the relations

$$
\left.
\begin{aligned}
q &= \left(\frac{2\pi}{2\pi - \tau}\right)^2 \sqrt{\frac{[(u+1)^2 + v^2]\,[(u-1)^2 + v^2]}{[(x+2)^2 + y^2]\,[(x-2)^2 + y^2]}\,\frac{(u^2 + u + v^2)^2 + v^2}{(u^2 + v^2)^{5/2}}} \\
&\quad \cdot \frac{\sqrt{(u^2 - u + v^2)^2 + v^2}\,\sqrt{u^2 + v^2 + 1 + 2u\cos(2p - 2\alpha) - 2v\sin(2p - 2\alpha)}}{u^2 + v^2 + 1 + 2u\cos p - 2v\sin p}, \\
\theta &= \alpha + 2\tan^{-1}\left[\frac{v}{u^2 + u + v^2}\right] - \tan^{-1}\left[\frac{v}{u^2 - u + v^2}\right] - \tan^{-1}\left[\frac{v}{u+1}\right] - \tan^{-1}\left[\frac{v}{u-1}\right] \\
&\quad - 2\tan^{-1}\left[\frac{u\sin p + v\cos p}{u^2 + v^2 + u\cos p - v\sin p}\right] + \tan^{-1}\left[\frac{y}{x+2}\right] + \tan^{-1}\left[\frac{y}{x-2}\right] \\
&\quad + \tan^{-1}\left[\frac{u\sin(2p - 2\alpha) + v\cos(2p - 2\alpha)}{u^2 + v^2 + u\cos(2p - 2\alpha) - v\sin(2p - 2\alpha)}\right].
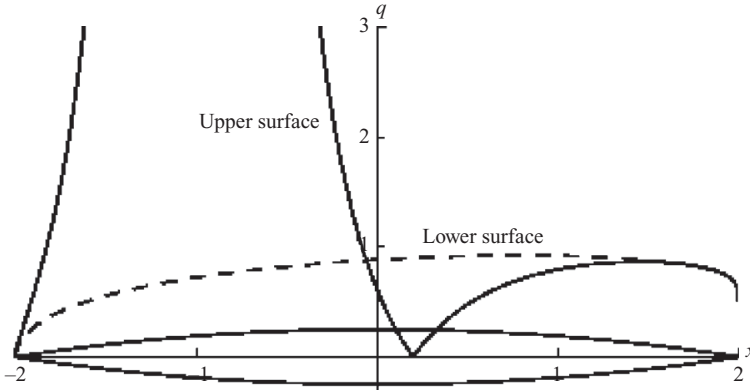\end{aligned}
\right\}
$$

$$(5.21)$$

A. Verhoff

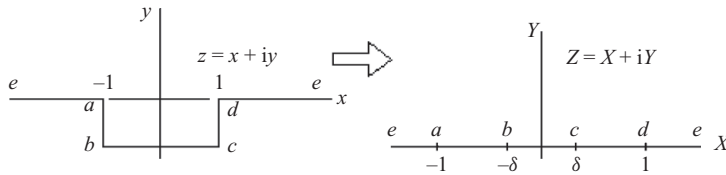FIGURE 33. Separated flow surface velocity ($\tau = .50$, $\alpha = 11°$).

FIGURE 34. Mapping to computational plane.

Surface velocity corresponding to the conditions of figure 29 (i.e. $\tau = 0.50$ and $\alpha = 11°$) is shown in figure 33.

This analysis can be extended to any blunt-nosed airfoil shape that can be mapped to the unit circle (e.g. general family of Karman–Trefftz profiles). The separation point location would have to be estimated from some additional analysis, such as boundary layer theory.

6. Rectangular cavity

Rectangular cavity geometries can be mapped onto the real axis of the computational Z plane by means of the Schwarz–Christoffel transformation, which defines the mapping function derivative as

$$\frac{\mathrm{d}z}{\mathrm{d}Z} = K\sqrt{\frac{1-Z^2}{\delta^2 - Z^2}}, \quad Z = X + \mathrm{i}Y. \tag{6.1}$$

Integration gives

$$z = K\,E(Z\,|\delta) + \text{const.}, \tag{6.2}$$

where $E(Z|\delta)$ represents the elliptic integral of the second kind. The factor K is a scaling parameter which can be chosen so that the lips of the cavity are located at $z = \pm 1$. The parameter δ controls the cavity depth. The real and imaginary parts of (6.2) provide x and y as functions of X and Y. As was the case in the backward-facing step analysis, simultaneous numerical inversion of (6.2) provides X and Y as functions of x and y. The mapping (6.2) is illustrated in figure 34. For a non-rectangular cavity where the front and rear vertical sides have different dimensions and the floor remains horizontal, the mapping is expressed as a combination of elliptic integrals of the first, second and third kind.
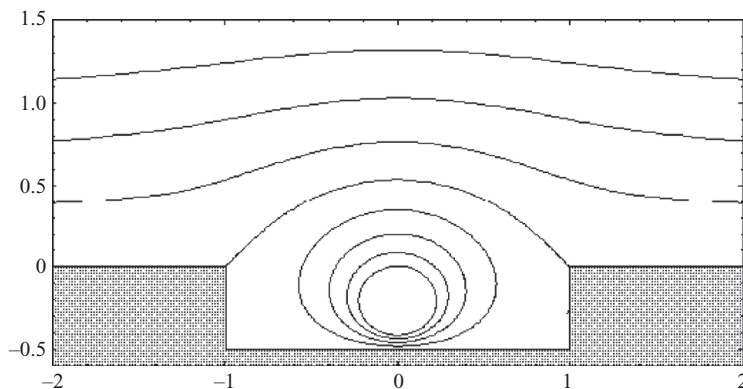
FIGURE 35. Separated flow streamline pattern (Aspect ratio $= .25$, $s = .20$).
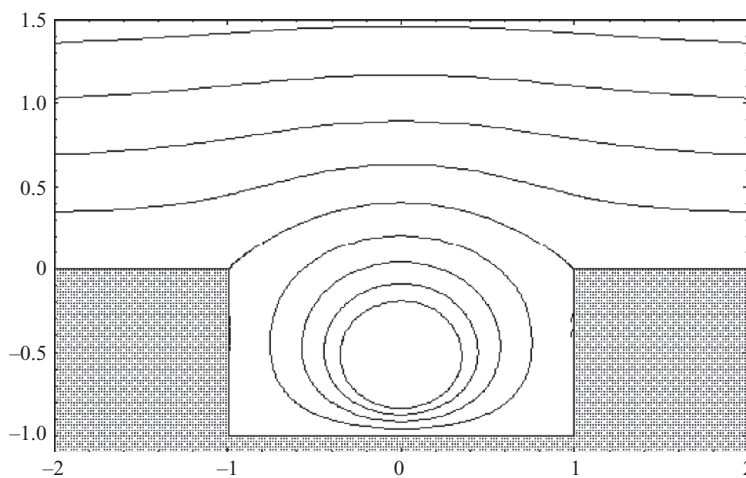
FIGURE 36. Separated flow streamline pattern (Aspect ratio $= .50$, $s = .20$).

Using the generalized vortex-pair model (4.13) and its component relations (4.14) in the Z plane, stream function contours can be mapped back to the z plane by the numerical inversion relations for X and Y mentioned above. Applicable parameter values are $p = 0$ and $b = -1$, while s remains arbitrary. Stream function contours are shown in figures 35 and 36 for cavity aspect ratios of 0.25 and 0.50, respectively, and for $s = 0.20$. The value of s changes the shape of the dividing streamline to a certain extent, but does not affect the streamline departure angles at the cavity lips. These angles are $\pm\pi/4$, and are a consequence of solutions of Laplace's equation.

7. Modelling extensions

The preceding models of separated flow and associated recirculation region typically relocate an infinite velocity singularity from the solid boundary to the centre of the recirculation region. The exception is the circular cylinder which has no boundary singularity. By moving the singularity 'out of the way', the solution becomes more realistic (but far from perfect), as far as surface conditions are concerned.

An obvious first extension would involve removing the vortical flow singularity. This can be done without undue effort by starting with a vortex pair model such as
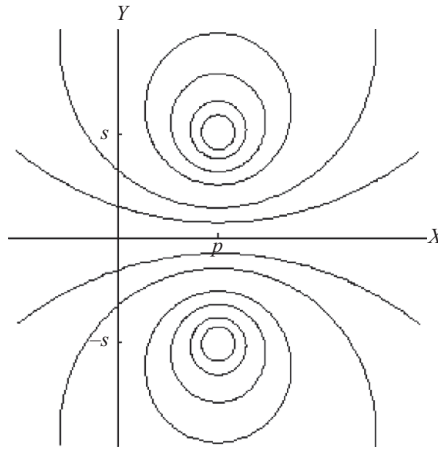
FIGURE 37. Vortex-pair streamline pattern.

(3.21). The flowfield of an isolated potential flow vortex located at $Z = p + \mathrm{i}s$ in the computational plane is described by

$$\Omega = \mathrm{i}\,K \log[Z - p - \mathrm{i}s]. \tag{7.1}$$

The vortex strength is K and the streamlines are concentric circles. Velocity is infinite at the centre and decays to zero in the far field.

If a second image vortex of equal strength but opposite rotation located at $Z = p - \mathrm{i}s$ is introduced, the resulting superimposed streamline pattern is as shown in figure 37. The closed streamlines remain circular but are no longer concentric. The pattern is symmetric about the X-axis, which can be replaced with a solid boundary. Superposition of a uniform flow in the positive X direction leads to the vortex-pair models (3.21) and (4.13).

Considering the upper half-plane flow pattern of figure 37, any of the closed circular streamlines (denoted by radius ρ) can be selected as a boundary between the outer potential flow and an inner core region where a solid-body-like rotational flow can be imposed in place of the potential flow. The exterior flow is unaffected by the size of the core region (i.e. ρ) and the inner region streamlines remain circular, although their numerical designation changes. The velocity distribution in the radial direction can be made continuous, but with a sharp peak (i.e. slope discontinuity) at the interface boundary. Additional details can be found in Rauscher (1953).

The velocity field of this extended model subsequently can be mapped to the physical z plane (e.g. to the backward-facing step configuration). Application of the mapping relation to the core region where the flow is rotational can be justified by the fact that the inner flow description is itself an approximation, and that the end result is an entire field free of singularities. The distortion of the core boundary depends on the potential flow solution and ρ, the core radius in the Z plane. The velocity (and pressure) distribution on the solid boundary likewise depends only on the potential solution.

A possible refinement to this extended model might employ some sort of viscous smoothing at the core boundary, applied in the computational Z plane, to remove the velocity slope discontinuity (i.e. sharp peak). In the Z plane the boundary is circular thereby simplifying the analysis. This would allow the influence of the core flow to

extend into the potential region to a certain degree. Some criterion (e.g. empirical) would need to be developed for the determination of ρ for a given class of geometries.

8. Discussion

Procedures have been demonstrated for obtaining two-dimensional incompressible potential flowfield solutions with separation and recirculation regions. Fixed separation and re-attachment points are not a requirement, depending on the geometry being considered. In certain situations, free solution parameters exist that may be approximately evaluated by appealing to experiment and/or viscous theory.

Use of flow angle to impose and manipulate boundary conditions makes for better overall understanding and allows ingenuity to play a role in extending the procedures to configurations other than those analysed herein. For certain geometries, solutions can be constructed using building-block elements, such as a doublet or vortex pair, bypassing a formal mathematical analysis.

Separated flow solutions have been presented for a backward-facing step, circular cylinder, rectangular cavity and biconvex airfoils. For the circular cylinder, analytical streamline patterns, when compared with experimental flow visualization graphics, show that major flowfield features are predicted reasonably well.

Prior to evaluating the utility of these simplified models for practical application, criteria must be developed for determining numerical values for the free parameters associated with various airfoil and cavity geometries and classes of bluff body shapes. For the circular cylinder results presented herein, crude selection of parameter values based on visual comparison with experimental results produced reasonably good correlation. Encouraged by this, empirical correlations for various geometry types appear to be a good starting point for this task. If these modelling procedures show promise as a framework for developing simple engineering prediction tools, then additional refinements would be in order. A simple procedure for removing the singularity within the vortical recirculation region by means of a core having solid body rotation has been outlined.

It is also hoped that this effort will spur some renewed interest in boundary layer theory, thereby providing insight into physical phenomena that only analytical solutions (guided by experiment) can offer. In the present context, separation point locations can be estimated by boundary-layer methods for smooth configurations without sharp corners that fix the separation point location. Likewise, inviscid dividing streamline (baseline) trajectories are well defined analytically for subsequent viscous shear layer analysis. Also of interest is the incorporation of flow angle boundary conditions into potential/Euler computational fluid dynamics (CFD) codes to asses their ability to duplicate the exact solutions presented herein. Comparisons with analytical solutions provide an excellent means for evaluating proper numerical implementation of boundary conditions (surface and far field) in these codes.

REFERENCES

BIRKHOFF, G. 1960 *Hydrodynamics*. Princeton University Press.
BIRKHOFF, G. & ZARANTONELLO, E. H. 1957 *Jets, Wakes, and Cavities*. Academic Press.
CHURCHILL, R. V. 1948 *Complex Variables and Applications*. McGraw-Hill.
GOLDSTEIN, S. 1957, *Modern Developments in Fluid Dynamics, Vol. I and II*. Oxford University Press.
IKEDA, T., ODA, T. & SHIBATA, T. 2004 *Proc. JSASS/JSME Struct. Conf.* **46**, 10.
JAMESON, A. 2003 *Paper 2003-3438*. AIAA.
KUETHE, A. M. & SCHETZER, J. D. 1959 *Foundations of Aerodynamics*. Wiley and Sons.

LAMB, H. 1932 *Hydrodynamics*. Cambridge University Press.

PRANDTL, L. & TIETJENS, O. G. 1934 *Fundamentals of Hydro- and Aero-Mechanics*. United Engineering Trustees, Inc.

RAUSCHER, M. 1953 *Aeronautical Dynamics*. Wiley and Sons.

SCHLICHTING, H. 1955 *Boundary Layer Theory*. McGraw-Hill.

VERHOFF, A. 1998 *AIAA J.* **36**, 148.

VERHOFF, A. 2005 *Paper 2005-5193*. AIAA.

YEUNG, W. W. H. & PARKINSON, G. V. 1993 *J. Fluid Mech.* **251**, 203.